


Ultrafast magnetic scattering on ferrimagnets enabled by a bright Yb-based soft x-ray source

G. FAN,^{1,2,3} K. LÉGARÉ,² V. CARDIN,² X. XIE,^{1,4}  R. SAFAEI,² E. KAKSIS,¹ G. ANDRIUKAITIS,¹ A. PUGŽLYS,¹  B. E. SCHMIDT,⁵ J. P. WOLF,⁶ M. HEHN,⁷ G. MALINOWSKI,⁷ B. VODUNGBO,⁸ E. JAL,⁸  J. LÜNING,⁸ N. JAOUEN,⁹ G. GIOVANNETTI,¹⁰ F. CALEGARI,^{3,10} Z. TAO,^{11,*} A. BALTUŠKA,¹ F. LÉGARÉ,² AND T. BALČIŪNAS^{1,6} 

¹Institute of Photonics, TU Wien, Gusshausstrasse 27/387, Vienna, Austria

²Institut National de la Recherche Scientifique, Varennes, Quebec J3X1S2, Canada

³The Hamburg Centre for Ultrafast Imaging CUI, Universität Hamburg, 149 Luruper Chaussee, 22761 Hamburg, Germany

⁴SwissFEL, Paul Scherrer Institute, 5232 Villigen PSI, Switzerland

⁵few-cycle, Inc., 2890 Rue de Beaurivage, Montreal, Quebec H1L 5W5, Canada

⁶GAP-Biophotonics, Université de Genève, 1205 Geneva, Switzerland

⁷Institut Jean Lamour, CNRS UMR 7198, Université de Lorraine, 54000 Nancy, France

⁸Sorbonne Université, CNRS, Laboratoire de Chimie Physique—Matière et Rayonnement, LCPMR, 75005, Paris, France

⁹Synchrotron SOLEIL, L'Orme des Merisiers, 91192, Gif-sur-Yvette, France

¹⁰Center for Free-Electron Laser Science CFEL, Deutsches Elektronen-Synchrotron DESY, Hamburg, Germany

¹¹State Key Laboratory of Surface Physics, Department of Physics, Fudan University, Shanghai 200433, China

*Corresponding author: Zhenshengtao@fudan.edu.cn

Received 18 October 2021; revised 16 January 2022; accepted 2 February 2022; published 6 April 2022

Development of ultrafast table-top x-ray sources that can map various spin, orbital, and electronic configurations and reordering processes on their natural time and length scales is an essential topic for modern condensed matter physics as well as ultrafast science. In this work, we demonstrate spatiotemporally resolved resonant magnetic scattering (XRMS) to probe the inner-shell 4d electrons of a rare-earth (RE) composite ferrimagnetic system using a bright >200 eV soft x-ray high harmonic generation (HHG) source, which is relevant for future energy-efficient, high-speed spintronic applications. The XRMS is enabled by direct driving of the HHG process with power-scalable, high-energy Yb laser technology. The optimally phase-matched broadband plateau of the HHG offers a record photon flux ($>2 \times 10^9$ photons/s/1% bandwidth) with excellent spatial coherence and covers the entire resonant energy range of RE's $N_{4,5}$ edges. We verify the underlying physics of our x-ray generation strategy through the analysis of microscopic and macroscopic processes. Using a CoTb alloy as a prototypical ferrimagnetic system, we retrieve the spin dynamics, and resolve a fast demagnetization time of 500 ± 126 fs, concomitant with an expansion of the domain periodicity, corresponding to a domain wall velocity of ~ 750 m/s. The results confirm that, far from cross-contamination of low-energy absorption edges in multi-element systems, the highly localized states of 4d electrons associated with the $N_{4,5}$ edges can provide high-quality core-level magnetic information on par with what can be obtained at the M edges, which is currently accessible only at large-scale x-ray facilities. The analysis also indicates the rich material-, composition-, and probing-energy-dependent driving mechanism of RE-associated multicomponent systems. Considering the rapid emergence of high-power Yb lasers combined with novel nonlinear compression technology, this work indicates potential for next-generation high-performance soft x-ray HHG-based sources in future extremely photon-hungry applications on the table-top scale, such as probing electronic motion in biologically relevant molecules in their physiological environment (liquid phase), and advanced coherent imaging of nano-engineered devices with $5 \sim 8$ nm resolution.

Published by Optica Publishing Group under the terms of the [Creative Commons Attribution 4.0 License](https://creativecommons.org/licenses/by/4.0/). Further distribution of this work must maintain attribution to the author(s) and the published article's title, journal citation, and DOI.

<https://doi.org/10.1364/OPTICA.443440>

1. INTRODUCTION

Understanding and controlling ultrafast light-induced spin dynamics have been developed into a fascinating research topic of condensed matter physics, motivated by both fundamental interests and technological applications. Time-resolved x-ray

techniques provide insights into spin changes with element specificity on their natural spatial and temporal scales [1]. Recently, the generation, control, and application of x-ray sources based on high harmonic generation (HHG) have received significant attention for time- and space-resolved spin dynamics measurements

utilizing magnetic dichroism sensitivity. In addition to being more compact and more accessible than large-scale x-ray facilities such as x-ray free-electron lasers (XFELs) and synchrotrons, table-top sources offer several unique advantages over them, particularly extremely short pulse duration [2,3], broad bandwidth (BW), and controllable spin [4–6] and orbital angular momentum [7,8]. Therefore, high-brightness HHG light sources [9–11] potentially serve as a unique laboratory-scale tool for the frontier of spintronic applications. Owing to its high spatial coherence, HHG radiation has been used for imaging of nanostructures with a large-scale view [12–14], magnetic imaging with diffraction-limited spatial resolution, and enhanced magnetic contrasts using holographic methods [15]. Furthermore, the extended degree of the control of spin [4–6] and orbital angular momentum [7,8] of HHG pulses via the manipulation of driving lasers provides the unique ability for resolving and controlling the magnetic and topological excitations of magnetic textures. Most importantly, HHG pulses enable femto-to-attosecond temporal resolution [2,3] for observing novel light-spin control phenomena in the unexplored sub-fs temporal regime [16]. The broad spectral BW of HHG spans the characteristic M- and N-absorption edges of transition metals (TM) and rare-earth (RE) elements that exhibit magneto-optical activity. Resonant x-ray probing at these edges [17] provides access to an element-specific [18] mapping of magnetic states and allows tracing their evolution in time.

Despite the numerous proof-of-concept demonstrations using HHG sources, all of the previous studies were focused on TM ferromagnets [19]. In contrast, recently developed magnetic nanostructure materials are based on ferrimagnetic/multiferroics multicomponent systems associated with RE [20–22] and are promising candidates for future storage and information processing spintronic devices owing to their nanometer size, fast speed, efficient driving dynamics, and topological protected stability [23]. Spontaneous emergence of magnetic order in nanoscale and mesoscale structures has been observed in TM-RE systems using x-ray scattering and diffraction techniques, and they play an important role in a variety of macroscopic phenomena in magnetic materials. Such heterogeneity of magnetic states in an otherwise spatially homogeneous material is a result of a complex interplay between electron spins and other degrees of freedom (electron orbitals and lattice). In particular, it has been shown that, after femtosecond laser irradiation, the exchange-coupled magnetic sublattices of particular TM-RE systems exhibit distinct magnetization dynamics of the constituent magnetic moments [20,24] and transfer of spin angular momentum between different sublattices [25], as well as between nanoscale spatial regions [26], which leads to a deterministic switching of sample magnetization on the femtosecond time scale [24,27]. Such space- and element-dependent ultrafast spin dynamics have been observed in, but not limited to, CoTb [25], (FeCo)Gd [28], and FeTb [29]. Furthermore, great progress has already been made in manipulating and detecting new structures, such as chiral textures and skyrmions. Recently, ultrasmall skyrmions (~ 10 nm) with fast dynamics at room temperatures in a compensated ferrimagnet have been resolved with time-resolved x-ray microscopy [23]. Since all these studies have relied on short wavelength x-ray probes at large-scale x-ray facilities, the development of novel x-ray techniques for element selective mapping of spin configurations and their fast reordering processes has still been a subject of intense research in the physics of magnetism over the last 10 years [1].

Soft-x-ray resonant magnetic scattering (XRMS) is a powerful x-ray technique combining diffraction with absorption spectroscopy that provides access to the complex charge, spin, and orbital orderings in materials [15]. It arises from an enhanced scattering amplitude when the incoming x-ray photon energy reaches the absorption edges of the constituent elements. XRMS is sensitive not only to magnetization distributions in the form of conventional domains but also to chiral spin texture structure [30,31], with spatial sensitivity down to few-nm scales [15]. Therefore, it can provide information unattainable through conventional visible [32], x-ray microscopy techniques and neutron scattering techniques. However, compared to spectroscopic methods, resonant magnetic scattering requires orders of magnitude higher photon flux because of the relatively low ($\sim 10^{-(5-6)}$) scattering cross section in the x-ray spectral range [33], which imposes a significant challenge for the application of HHG sources for these types of scattering experiments. Another fundamental bottleneck is the cross-contamination of the peaks (e.g., M edge of TM and O edge of RE) in complex multicomponent TM-RE systems at low x-ray photon energies [34], where the many-body corrections and local field effects are of crucial importance. It worth to note that high-energy and high-flux XFELs allow precise measurement of magnetic scattering in a large momentum space, which leads to high spatial resolution, but the applications are limited by the cost and available beamtime. For an HHG-based instrument, to image the laser-induced nanoscale spin dynamics and the transfer in association with the magnetic sublattices in TM-RE ferrimagnets, it is crucial to extend HHG photon energy to cover the inner-shell absorption edges of 4d RE ferrimagnets (Gd, Tb, and Dy). While considerable progress has been made to extend the phase-matched HHG cutoff with longwave driver pulses from optical parametric amplifiers (OPAs) [35–41], it came at the expense of efficiency in the soft x-ray spectral range because scaling the wavelength of the driver pulses (λ_L) reduces the single-atom HHG yield [42] to $\lambda_L^{5.5 \pm 0.5}$, and because of the low conversion efficiency of OPAs (10%–20%). On the other hand, the recent development of novel Yb laser sources [43–45] is showing great potential for next-generation driver technologies of HHG, owing to the advantages of high power scaling, robustness, and compactness. A proof-of-concept HHG source using a high-repetition-rate Yb fiber driver has been demonstrated [46]. A novel energetic multidimensional-solitary states (MDSS)-based post-compression technique has been discovered, showing huge potential to further scale the performance of Yb lasers [47]. Nevertheless, so far, spatiotemporally resolved element-specific probing of RE magnetic systems in the soft x-ray spectral range has remained inaccessible with table-top HHG sources.

In this work, we demonstrate, for the first time, time-resolved XRMS (tr-XRMS) based on a high-brightness Yb-based HHG source at the $N_{4,5}$ edges of RE elements, which corresponds to a dipole allowed 4d-to-4f transition. This high-brightness soft x-ray source is accomplished by directly driving the HHG process in the optimally phase-matched regime in helium by using a power scalable, kHz, high-energy, 1030 nm, Yb laser system with a peak power of 0.3 TW. The HHG cutoff reaches up to 220 eV, and the phase-matched broadband plateau of the high-brightness HHG source with record flux ($> 2 \times 10^9$ photons/s/1% BW) is especially suitable for the photon demanding tr-XRMS at the $N_{4,5}$ edges of REs (Gd, Tb, and Dy). Furthermore, the relatively long propagation distance of the nearly quasi-plane-wave driver

laser field in the optimally phase-matched conditions results in a low-divergence and high-spatial-coherence soft x-ray beam, which is particularly important for high-quality spatially resolved tr-XRMS measurements. To investigate the intrinsic energy transfer efficiency from the IR driver to the generated soft x rays for the desired resonance energy range at the RE N edge, we experimentally compare various generation schemes by employing different wavelengths, gases, and pressures. The underlying physics for efficient HHG is verified with a theoretical analysis combining the microscopic electron wave packet trajectories and macroscopic phase-matching process. We perform table-top tr-XRMS measurements on a prototypical CoTb ferrimagnet by covering the $N_{4,5}$ edges of Tb around ~ 155 eV. From the time-resolved scattering patterns, we retrieve the demagnetization evolution of the localized $4d$ electron associated with the $N_{4,5}$ edges exhibiting a demagnetization time of 500 ± 126 fs originating from the fast-electronic heating. This has so far been observed only at the M edges of RE materials using hard x-ray pulses at large-scale facilities [25]. Furthermore, we observe the laser-induced evolution of nanoscale magnetic domains on the femtosecond time scale, which we compare with results from previous studies [48,49], revealing the potential role of complex material-, composition-, and, possibly, probing-energy-dependent driving mechanisms of RE-associated multicomponent systems.

2. RESULTS

The schematic of the experiment is illustrated in Fig. 1. We focus on the highly localized states of $4d$ electrons associated with the $N_{4,5}$ edges of Tb using a bright, soft x-ray table-top source at 155 eV, allowing to probe the inner-shell electron spin states. We show that probing at the N edge via tr-XRMS provides rich information on the magnetic properties that are as accurate as probing at the M_5 edge at 1240 eV. This comes from the fact that $4d$ electrons are sufficiently shielded, and N-edge transitions are free of the complex cross-contamination [34] of peaks in TM-RE systems in contrast to the O_1 edge at lower photon energies (from 50 eV to 70 eV), where the manybody corrections and local field effects are of crucial importance [Fig. 1(b)]. The core of the experimental setup is shown in Fig. 1(a). The fundamental femtosecond pulses with $\lambda_L = 1030$ nm and a duration of ~ 220 fs from a Yb : CaF₂ amplifier were first compressed by a post-pulse compressor, consisting of a hollow-core fiber (HCF) and a set of chirped mirrors. The implemented HCF is 3 m long and has a large core diameter (1 mm), enabling a compression ratio of ~ 10 for the high-energy (~ 11 mJ) pulses. The post-compressed pulses have a peak power of ~ 0.3 TW (25 fs, 8 mJ), which is key for achieving efficient laser-like HHG [Fig. 2(c)] up to 220 eV in a 20 mm helium-filled gas cell with adjustable backing pressure. The harmonic spectrum is characterized by a soft x-ray spectrometer. As shown in Figs. 2(a) and 2(e), the change of the pulse duration from 220 fs to 25 fs extends the HHG cutoff from 150 eV to 220 eV. Particularly, the photon flux at the desired resonance of the Tb $N_{4,5}$ edge is increased by over one order of magnitude. This result can be explained by the suppression of ionization for a shorter driver pulse.

A. Development of the High-Brightness Soft X-Ray HHG Source

To generate high-brightness HHG radiation, it is essential to reach optimal phase-matching conditions by routinely optimizing

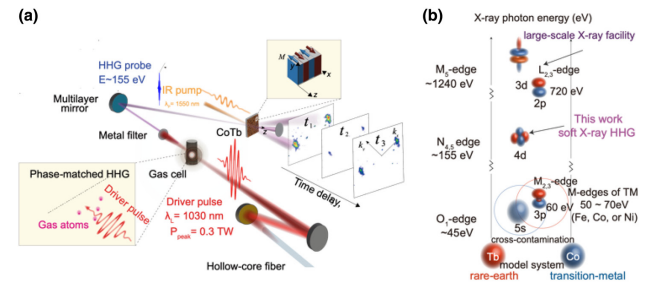


Fig. 1. Schematics of the Tr-XRMS experiment using soft x-ray HHG source. (a) High-brightness high-order harmonics are generated in a gas cell filled with helium and driven by compressed pulses in the optimal phase-matching conditions. Tr-XRMS experiments are carried out in a pump-probe geometry by exciting the sample with IR pulses with a wavelength of 1550 nm before HHG probe pulses arrive. The spatiotemporal evolution of the magnetic domains is measured with time-resolved diffraction patterns from the harmonic beam, recorded with a CCD camera as a function of the delay time. (b) Illustration of the x-ray energies of different absorption edges of TM and RE elements. The low-energy O_1 edge of RE and the $M_{2,3}$ edges of TM are close in energy, which could be challenging to distinguish in experiments. The high-energy $M_{3,4}$ edges of RE and $L_{2,3}$ edges of TM, on the other hand, require a large-scale x-ray facility. Our solution lies in between and can provide a table-top source probing the magnetic dynamics with the $N_{4,5}$ edges of RE.

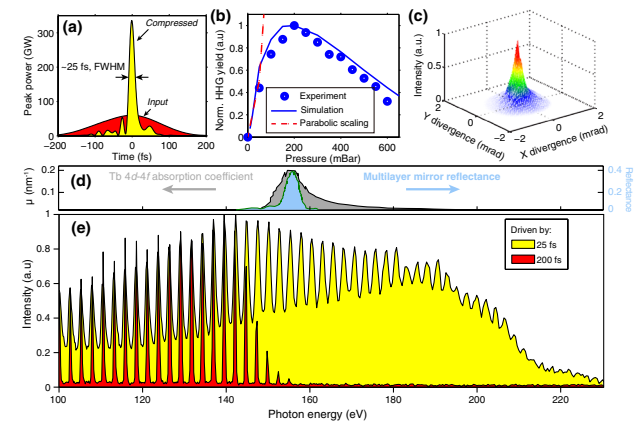


Fig. 2. Driver pulse compression and HHG characterization. (a) Temporal characterization of uncompressed and compressed driver pulses with the frequency-resolved optical gating (FROG). (b) Measured and simulated HHG signals as a function of the helium backing pressure with a peak power of ~ 0.3 TW at a wavelength of 1030 nm. (c) Beam profile of the narrowband harmonic beam after the multilayer mirror with a central photon energy of 155 eV. (d) Absorption cross section of Tb near its $N_{4,5}$ edge [50] and the reflectance of the x-ray multilayer mirror. (e) High-order harmonic spectra driven by uncompressed (200 fs) and compressed (25 fs) pulses.

the gas pressure, focusing conditions, position of the cell, etc. In Fig. 2(b), we plot the total spectrum intensity for photon energy > 100 eV as a function of the backing pressure of helium, at a peak intensity of 6.5×10^{14} W cm⁻². The HHG intensity grows quadratically at low backing pressures, followed by a saturation of the signal at a backing pressure of 200 mbar. When further increasing the pressure, the spectral intensity decreases due to the absorption of the generated harmonics within and after the generation volume. This observation is reproduced with high fidelity in our *ab initio* simulation based on the strong-field approximation [see Fig. 2(b) and Supplement 1]. We further optimize the

gas-cell length and find that the HHG flux saturates when the length is larger than 20 mm, indicating the absorption-limited HHG condition [51]. As shown in Fig. 2(e), we observe a flat-top spectrum covering the broad spectral range up to a cut-off energy of ~ 220 eV. This value is in excellent agreement with the predicted HHG phase-matching cutoffs for $\lambda_L = 1030$ nm [11]. Compared to previous experiments [46,52], the high peak intensity of the driving laser here allows us to use a loose focusing geometry and relax the requirements on the phase-matching pressure.

To verify the advantages of our generation strategy for obtaining a high photon flux within the range of the $N_{4,5}$ edges of RE elements, we experimentally compare the conversion efficiency of our approach: (i) $\lambda_L = 1030$ nm in helium with two other generation schemes based on OPAs: (ii) $\lambda_L = 1500$ nm in neon, and (iii) $\lambda_L = 2400$ nm in argon. We adjust the peak power, pulse duration, and focusing geometry of the driving laser in every case to reach the same cut-off energy. For gases with a lower ionization potential, it is essential to use a long-wave driver pulse to stay below the critical ionization level. The backing pressure of the gas medium is also optimized to obtain phase-matched and absorption-limited HHG. The absolute HHG flux right after the gas cell for case (i) ($\lambda_L = 1030$ nm in helium) is estimated under diffraction geometry by considering the known efficiency of the CCD (Andor Newton 920), the transmission of the 500 nm zirconium filter ($\sim 15\%$), and BW and efficiency ($\sim 3\%$) of the EUV multilayer mirrors. The photon fluxes for the other conditions are then calculated according to the relative spectral intensity measured using the same spectrometer. Conversion efficiency is then calculated by considering the input pulse energy in each case (see Supplement 1). The experimentally measured conversion efficiencies for the three different approaches are plotted in Fig. 3(a), showing that our method [(i) $\lambda_L = 1030$ nm in helium] yields the highest conversion efficiency throughout the $100 \sim 200$ eV range of interest, which is supported by our simulations shown in Fig. 3(b).

For the phase-matched HHG, absorption-limited conversion efficiency can be described as $\xi_q = \lambda_L^{-n} |A_q|^2$ [51], where A_q is the amplitude of the single-atom recombination cross section at the harmonic frequency ω_q , λ_L^{-n} represents wavelength scaling due to the electron wave packet diffusion during its free-space excursion, with $n = 5.5 \pm 0.5$ [42], and σ is the x-ray absorption cross section. As shown in Fig. 3(c), the longest electron wave packet excursion occurs for argon with $\lambda_L = 2400$ nm, which leads to a significant reduction in recombination probability for case (iii) [11]. In contrast, the single-atom responses for (i), $\lambda_L = 1030$ nm in helium, and (ii), $\lambda_L = 1500$ nm in neon, are similar since the stronger wave packet diffusion for the longer λ_L is compensated for by the larger recombination cross section associated with the larger ionic core of neon in case (ii). Summarizing the above discussion of microscopic single-atom response, the expected HHG efficiency is similar for both helium and neon. Nevertheless, macroscopic propagation changes the situation in favor of helium because its x-ray absorption cross section (σ) is one order of magnitude lower than neon at the energy of 200 eV [Figs. 3(a) and 3(b)]. For a fixed driver pulse duration, this simple model suggests a straightforward recipe for reaching the highest flux at a target x-ray photon energy located in a resonance-free plateau region of the harmonic spectrum in the vicinity of the cutoff. The highest efficiency is achieved using helium driven by the shortest laser wavelength capable of reaching the corresponding

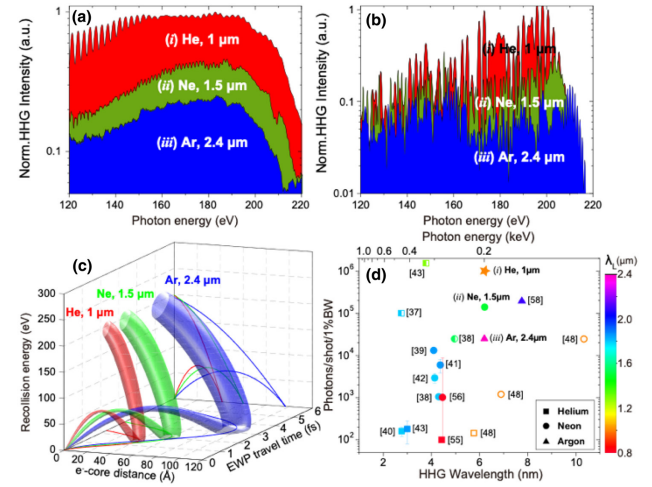


Fig. 3. High brightness of HHG directly driven by compressed 1030-nm-wavelength laser pulses. (a) Measured and (b) simulated conversion efficiencies of HHG in the $100 \sim 200$ eV spectral range generated in (i) helium with $\lambda_L = 1030$ nm, (ii) neon with $\lambda_L = 1500$ nm, and (iii) argon with $\lambda_L = 2400$ nm. The peak power, pulse duration and focusing geometry are adjusted to yield the same cut-off energy of the spectra. The conversion efficiencies in (a) and (b) are all normalized to the conversion efficiency in case (i) at ~ 200 eV. (c) Simulated cut-off trajectories for the three cases shown in (a) and (b). The radii of the trajectories linearly increase with the excursion time, symbolizing wave packet spreading. The more efficient single-atom response for $1 \mu\text{m}$ in helium is due to reduced electron wave packet (EWP) spread caused by the shorter wavelength driving field. (d) Overview of the experimentally generated HHG flux in photons per shot per 1%BW above 100 eV in helium (squares) [35,38,41,46,53], neon (circles) [36–38,40,46,54,55], and argon (triangles) [56]. The driving field wavelength (λ_L) is illustrated by marker colors. The repetition rate of HHG is at ~ 100 kHz for open symbols, at $10 \sim 50$ Hz for the half-filled symbols, and at ~ 1 kHz for the fully filled symbols.

semi-classical cutoff, given that the laser pulse intensity is sufficient to sustain a phase-matched HHG regime.

In Fig. 3(d), we show that, owing to the high conversion efficiency for the HHG driver wavelength of 1030 nm in helium, we achieve the highest flux of 2×10^9 photons/s/1%BW at 200 eV (see Supplement 1). Unlike most previous experiments summarized in Fig. 3(d), in which λ_L -dependent cut-off extension was studied, our method is free of additional energy loss due to the absence of parametric frequency conversion. Reviewing HHG results with direct laser driving at different wavelengths, it must be noted that with laser pulses of $\lambda_L = 800$ nm from a Ti:sapphire amplifier, it is possible to extend the cutoff beyond 200 eV by employing sub-10 fs driver pulses [55] or using quasi-phase-matching techniques [54]. However, in these situations, ionization-induced phase mismatch quickly outruns the dispersion contribution of neutral atoms, making macroscopic phase matching very challenging [57]. In contrast, in our experiments with driver pulses of $\lambda_L = 1030$ nm, we significantly suppress the ionization of helium, thus facilitating phase matching. The estimated ionization fraction is below 0.38%, while the critical ionization of helium is 0.4%. We also note that a photon flux $> 10^9$ photons/s/1%BW is not necessarily rare at photon energies < 100 eV, which can be readily used for tr-XRMS studies on the low-energy $M_{2,3}$ edges of TM elements [58].

B. First tr-XRMS Measurement Covering the N Edge of RE

In previous studies, owing to the rapid development of ultrafast x-ray sources, time-resolved element-specific absorption spectroscopy and resonant scattering measurements were used for studying ultrafast demagnetization in ferro- and ferrimagnetic alloys or multilayers. By probing on different magnetic elements, distinct laser-induced magnetic dynamics were revealed, owing to the exchange interaction and transfer of spin angular momentum between elements. López-Flores *et al.* studied the ultrafast demagnetization in Co-RE alloys (RE = Gd, Tb) using a femtosecond-slicing source covering the $M_{4,5}$ edges of RE elements, and showed that the demagnetization dynamics are element and composition dependent [25]. On the other hand, Merhe *et al.* studied the ultrafast demagnetization and changes in domain structure in CoTb alloys by covering the low-energy O_1 edge of Tb [59] using a similar source. Their results presented evidence for domain-wall broadening, while, more interestingly, they reported a faster demagnetization time compared to Ref. [25], which implies that different dynamics may depend on the probing photon energy. More recently, by covering the M_5 edge of Tb, Ferté *et al.* reported ultrafast demagnetization of CoTb alloys by hot-electron excitation [60]. Besides the above results, dynamics of the magnetic domains have been studied by covering the M_3 edges of TM elements in Co/Pd and Co/Pt multilayers, but they have yielded very different behaviors [48,49]. We note that most of the above experiments were performed using XFELs, and that results on the $N_{4,5}$ edges of RE elements are still absent, to the best of our knowledge.

The concept of HHG-based tr-XRMS for temporally and spatially resolving spin dynamics at the $N_{4,5}$ edges of RE elements is illustrated in Fig. 4. One important advantage of this method is the ability to use linearly polarized HHG to retrieve high-quality x-ray magnetic circular dichroism (XMCD)-related information from the magnets. Indeed, the production of circularly polarized HHG requires additional rather complex driver setups. It also requires very high purity of the circularity of the driver laser pulses, because any imperfection of the circularity from the fundamental driver beam will be enhanced and transferred into the generated circularly polarized x-ray beam in the soft x-ray regime [61]. The underlying fundamental physical processes of using linearly polarized x-ray light to enable strong magnetic contrast is illustrated in Fig. 4. It can be intuitively understood in terms of these different scattering amplitudes $E_{RC,LC}$ for the opposite helicity circular components that form the linearly polarized beam, or in other words, linearly polarized x-ray light can be seen as the superposition of two opposite helicities (right circularly and left circularly polarized x-ray light) that are differently scattered by magnetic domains depending on the magnetization orientation [15] (see Supplement 1). The quantitative clarification of the physical origin of XRMS by using circularly polarized x-ray light and its link to the conventional XMCD measurements have already been developed using an eigenwave formalism [62]. The actual refractive indices and their energy dependence with linearly polarized x-ray light around a core level are calculated by following a classical description of Maxwell equations and a permittivity built from the quantum scattering amplitude [62]. The inference of the x-ray beam encoding with different refractive index information will form a scattering pattern in the far field, which can be characterized through the scattering

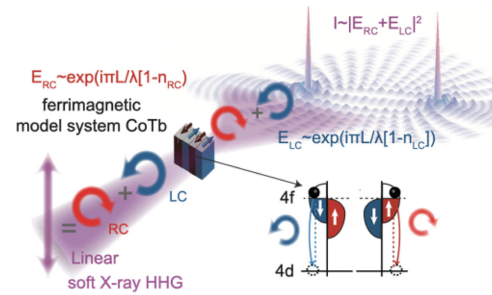


Fig. 4. Illustration of the physical mechanism of XRMS at the $N_{4,5}$ edges of REs using linearly polarized soft x-ray HHG source. The linearly polarized x-ray light can be regarded as the superposition of two circularly polarized light fields with opposite helicities. At the absorption edge of the element, the magneto-optical effect can be analogous to circular dichroism in absorption. The magnetic nanodomain structure of the sample can be approximated by a grating in which the transmission of each domain depends on the relationship between the orientation of the magnetic moment and the helicity of the incoming beam.

vector, applied light field, and spectral dependences in reciprocal space. We note that the diffraction patterns come from the leading term for XRMS, $(\mathbf{e}_f \times \mathbf{e}_0) \cdot \mathbf{m}$, where \mathbf{e}_0 and \mathbf{e}_f represent the polarization unit vectors of incident and scattered light, respectively, and \mathbf{m} is the sample magnetization [59,63] (see Supplement 1).

Here, we carry out the first table-top tr-XRMS measurements, reaching the $N_{4,5}$ edges of Tb, in a CoTb sample prototypical of TM-RE ferrimagnetic alloys. The sample is a 50 nm film grown on a Si_3N_4 membrane and exhibiting an out-of-plane magnetic anisotropy with a striped domain structure. We note that, even though the $N_{4,5}$ edges of Tb are tabulated at 150.5 eV, defining the absorption threshold of the $4d$ to $4f$ transition, the highest diffraction efficiency occurs at the energy of ~ 155.5 eV, which was confirmed by measurements on the same samples at the SOLEIL synchrotron and also by previous experiments with higher-energy resolution [50] [see Fig. 5(a), and Supplement 1]. As a result, a concave multilayer mirror with a central energy of ~ 155 eV and a 5-eV-wide BW was selected to focus the harmonic beam onto the ferrimagnetic prototype sample.

The measured static XRMS pattern of the sample is shown in Fig. 5(c). Through XMCD sensitivity [59,63], the alternating oppositely magnetized domains [Fig. 5(b)] effectively serve as a diffraction grating for the incident linearly polarized soft x-ray beam set at a resonant wavelength of ~ 8 nm, which can be decomposed as two circularly polarized fields with opposite helicities, giving rise to the clear plus-and-minus first-order diffraction peaks in the far field. We simulate the scattering intensity by using a resonant wavelength of Tb $N_{4,5}$ edges (~ 8 nm) with a 0.8 nm BW with a normalized mutual coherence factor of one, which describes the internal correlations between the wavefront phases of the beam at different locations [Fig. 5(d)]. The obtained real-space stripe-like diffraction pattern from the simulation consists of two well-defined diffraction spots, which have good agreement with the experimentally measured XRMS pattern. The agreement is not only because of the small wavelength of the x-ray but also because of the longitudinal coherence (monochromaticity) of the beam. For phase-resolved applications, such as large-scale view nanoimaging [12–14], and enhanced magnetic contrasts using holographic methods [15], spatial coherence is also important. Note that since HHG is an “electron recollision” process in the microscopic picture

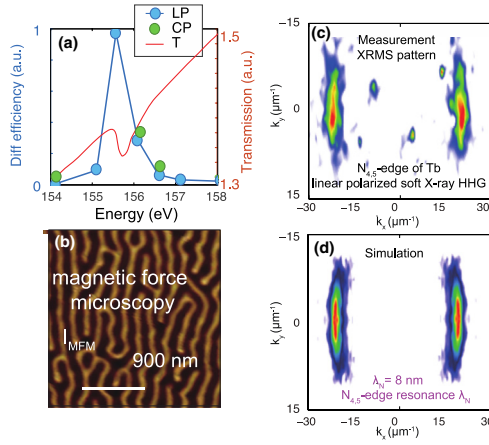


Fig. 5. XRMS measurements and simulations of the CoTb sample at the N edge of Tb. (a) Soft x-ray diffraction efficiency as a function of the photon energy of our sample measured at SOLEIL synchrotron. LP, linearly polarized; CP, circularly polarized; T, transmission. (b) Magnetic domain structure of the same CoTb sample measured using a magnetic force microscope (MFM). (c) Experimentally measured XRMS pattern as a function of momentum transfers k_x and k_y , corresponding to the magnetic domains. (d) Simulated scattering intensity of XRMS pattern of the sample, assuming a magnetic domain network with opposite out-of-plane magnetization directions, and homogeneous charge distribution at $N_{4,5}$ edges of Tb using linearly polarized x-ray light at a wavelength of 8 nm (155 eV). The mutual coherence factor was chosen as one.

[64], particular x-ray photon energies can be generated through different electron trajectories in the optical cycles of the driver laser field, which may lead to a reduction in spatial coherence. In our case, the optimally phase-matched condition in the long gas cell with a high driver laser pulse peak power (0.3 TW) leads to a nearly quasi-plane-wave interaction and a long propagation distance in the nonlinear medium, which is favorable to select a single recollision trajectory and serves to provide high mode quality [nearly Gaussian-like, low divergence <2 mrad, Fig. 2(c)] and spatial coherence [65]. Furthermore, since the length scales of magnetic domains are much larger than the wavelength of the incoming x-ray beam and we do not observe notable differences in the simulated patterns of the resonant wavelength at the N edge and the one at the M edge, this indicates, for the present sample, that the resonant wavelength of ~ 8 nm ($N_{4,5}$ edge) provides spatially resolved high-quality information that is as good as the M_{5} -edge resonance wavelength of ~ 1.1 nm, which would require high-energy facility-scale sources. Our soft x-ray ~ 8 nm HHG source with excellent spatial coherence can potentially provide diffraction-limited resolution [66], and we emphasize that this is particularly attractive for resolving recently discovered ultrasmall structures (~ 10 nm) in TM-RE systems [22,23].

The ultrafast dynamics in the prototype ferrimagnets of CoTb are induced by pump laser pulses with a wavelength of 1550 nm and pulse duration of 80 fs obtained from an OPA driven by the same Yb driver laser and are probed by soft x-ray pulses arriving at the sample with a time delay. The overall time resolution of our system is ~ 84 fs, defined by the convolution of the pump and soft x-ray probe pulse duration. Here, the pulse duration of the soft x-ray probe is assumed to be nearly the same as compressed laser pulses (25 fs), since soft x-ray radiation is generated within the half-cycle of the laser pulses. The domain magnetization amplitude M can be measured as the square root of diffraction intensity, while the

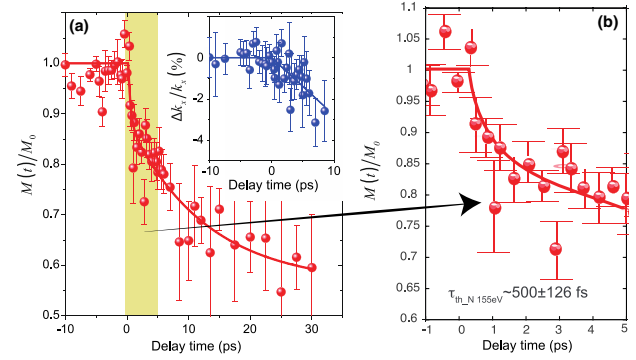


Fig. 6. Time-resolved XRMS measurements of the CoTb sample at the $N_{4,5}$ edge. Variation of the averaged magnetization $M(t)$ as a function of the pump–probe delay time in (a) 35 ps scan range and (b) 5 ps scan range. The magnetization amplitude is extracted from the time-dependent variation of the intensity of the XRMS diffraction patterns and is normalized to the ground-state magnetization M_0 . (c) Change in momentum transfer in the x direction in percentage ($\Delta k_x/k_x$) as a function of delay time.

spatial evolution of the magnetic domains is revealed by the change in momentum transfer (Δk) [48]. As shown in Fig. 6(a), with a pump fluence of $8 \text{ mJ}/\text{cm}^2$, the intensity of the diffraction peaks is suppressed by $\sim 70\%$, which corresponds to demagnetization up to $\sim 50\%$. The demagnetization of the sample exhibits two time scales: an ultrafast demagnetization process quickly suppresses $\sim 10\%$ of the sample magnetization in the sub-ps scale, followed by a slow demagnetization process in several tens of ps. The two-step process is consistent with the type II demagnetization dynamics previously observed for RE materials, including pure Tb [67], FeTb [68], $\text{Gd}_{1-x}\text{Tb}_x$ alloys [69], and CoTb alloys [59].

To quantitatively determine the characteristic time constants of the processes involved in the measurements, we use a double-exponential fit function convoluted with the time resolution of the experiment $G(t)$ of 84 fs:

$$f(t) = G(t) * \left[A - B \times \left(1 - \exp\left(-\frac{t}{\tau_1}\right) \right) - C \times \left(1 - \exp\left(-\frac{t}{\tau_2}\right) \right) \right],$$

where A is the value of the transient signal at negative delays, and B and C are exponential amplitudes. From this fitting, we can retrieve two important time constants τ_1 and τ_2 from our measured data at the $N_{4,5}$ edge of Tb, which are defined, respectively, as the initial rapid drop of sample magnetization with a thermalization time involving hot electrons and the relaxation time from the spins to other degrees of freedom (lattice, external bath). The obtained fast demagnetization time constant τ_1 at the $N_{4,5}$ edges of Tb is $\tau_{Tb-N} = 500 \pm 126$ fs.

Very interestingly, we find that the fast demagnetization time scale here [Fig. 6(b)] is in a good agreement with previous results probing the M_5 edge of Tb [25] (using a large-scale x-ray facility), but slower than that obtained by probing at the O_1 edge [59]. This difference could be attributed to the different initial states probed in these experiments, given that the d states of N and M edges are highly localized, while the 5s states corresponding to the O edge are more delocalized, which implies different magnetic dynamics possibly depending on probing energy [59]. On the longer time

scale, we find that sample magnetization does not recover even at ~ 100 ps after pump excitation, which has been typically observed in many ferro- and ferrimagnetic materials containing RE elements [59,67–69].

As shown in Fig. 6(c), the momentum transfer (k) in the x direction is reduced by $\sim 3\%$ in ~ 10 ps after pump laser excitation (see Supplement 1). We note that the decay of Δ/k is much slower than the sample demagnetization ($M(t)/M_0$) and can be approximated as a linear decrease as a function of time. If we assume that the shift of the scattering peaks is correlated to the expansion of the domain periodicity, the slope of the change yields a velocity for the domain walls of ~ 750 m/s. In past works, the dynamics of magnetic domain structures in ferromagnetic multilayers, containing TM elements, have been studied with tr-XRMS with HHG and XFEL sources [48,49,59]. Different materials and compositions yield different dynamics: it was found that the magnetic domains in Co/Pd multilayers remain mostly unaffected by laser-induced demagnetization [48], while the variation of magnetic domains coincides with the demagnetization dynamics in Co/Pt multilayers [49]. In particular, Pfau *et al.* reported the softening of the domain wall owing to the ultrafast spin diffusion process, which results in an almost simultaneous shift of the momentum transfer accompanied by the demagnetization dynamics [49]. Our results here, however, show a much slower domain dynamic, indicating that the ultrafast spin diffusion is unlikely to be the driving mechanism.

On the other hand, Merhe *et al.* suggested that the decrease in uniaxial anisotropy in CoTb alloys after the laser-induced lattice heating may be responsible for the domain-wall expansion [59]. However, this does not occur in the first 4 ps, until the lattice is heated up, which is obviously different from what we observe here. The discrepancy between our observation and previous results indicates that the domain dynamics here must be driven by a different mechanism, which could be material, composition, and possibly probing energy dependent. More experiments and sophisticated theoretical modeling will have to be developed in the future to give a better understanding of the ultrafast spatial dynamics of magnetic domains in TM-RE ferrimagnetic systems. The tr-XRMS system based on our high-brightness and high-energy HHG soft x-ray source could provide a valuable platform to perform such studies.

3. DISCUSSION AND CONCLUSION

We experimentally and theoretically investigate a HHG scheme for spintronic applications that provides a soft x-ray beam with low divergence (< 2 mrad), outstanding spatial coherence, and record photon flux ($> 2 \times 10^9$ photons/s/1% BW) up to > 200 eV. This soft x-ray HHG source enables us to perform tr-XRMS measurements on a CoTb ferrimagnetic alloy, reaching the $N_{4,5}$ edges of Tb for the first time. According to the experimental results, we observe laser-induced ultrafast demagnetization on femtosecond time scales, as well as a shift of scattering peaks that indicates dynamics in the domain structure, indicating the rich driving mechanisms of RE-associated multicomponent systems. We note that, before our work, similar experiments could be carried out only at XFELs and femtosecond-slicing facilities. Our results suggest that, by avoiding the cross-contamination of low energy absorption edges in multi-element systems, N edges can provide high-quality core-level magnetic information of TM-RE systems.

The scheme of the demonstrated generation method in the wavelength of $5 \sim 8$ nm can provide new possibilities for realizing

ultrafast spin manipulation and ultrafast imaging of magnetic nanostructures [66,70]. This is important for building functional skyrmion devices that can be written, read, manipulated and erased in a deterministic way in the future [71], and this will open new opportunities for electrically controlled topological electronics and spintronics. Furthermore, the unique capability of generating attosecond soft x-ray pulses with high brightness will pave the way for observing sub-femtosecond all-optical spin control in a much wider variety of magnetic materials [16].

Today, the new high-power ultrafast Yb laser technology is emerging rapidly. Yb-based fiber- [43], slab- [44], and thin-disk [45] lasers at several hundred or even kilowatt average power are becoming commercially available. Novel nonlinear compression is drawing significant research efforts to boost further the sub-ps Yb laser performance (in terms of peak power, duration, wavelength), e.g., solitons in periodic layered Kerr media with high compactness accompanying self-cleaning of the beam [72], and energetic multidimensional solitary states (MDSS) in the HCF enabling unexpected compression factors and sufficient wavelength tunability [47]. Considering such newly achieved driver technology, the photon flux of HHG can be further scaled by another several orders of magnitude in the soft x-ray spectra range, accompanied by a compact and robust architecture. The high-performance table-top HHG source will continue to be at the forefront of many scientific breakthroughs, opening doors in exciting interdisciplinary research in various fields, including condensed matter physics, life sciences, and nanotechnology [12].

Funding. Deutsche Forschungsgemeinschaft (Cluster of Excellence Advanced Imaging of Matter); Fonds de recherche du Québec – Nature et technologies; Natural Sciences and Engineering Research Council of Canada; Shanghai Municipal Science and Technology Basic Research (19JC1410900); National Key Research and Development Program of China; National Natural Science Foundation of China (11874121); Institut national des sciences de l'Univers (CNRS-MOMENTUM); Agence Nationale de la Recherche (UMAMI ANR-15-CE24-0009); Austrian Science Fund (P30465-N27, FWF P27491); Marie Skłodowska-Curie (798176).

Acknowledgment. Z.T. gratefully acknowledges the financial support from National Key R&D Program of China, the National Natural Science Foundation of China, the Shanghai Municipal Science and Technology Basic Research Project, and the Alexander-von-Humboldt Foundation. T.B. acknowledges funding from the EU H2020 research and innovation program under the Marie Skłodowska-Curie Actions. X. Xie acknowledges funding from the Austrian Science Fund (FWF) (P30465-N27). G. F. T.B and A.B acknowledge funding from the Austrian Science Fund (FWF) (FWF P27491). M.H., G.M., B.V., and J.L. thank the French Agence Nationale de la Recherche for support via projects UMAMI ANR-15-CE24-0009. E.J. is grateful for the financial support of the CNRS-MOMENTUM program. F.L., G.F., K.L. V.C., and R.S. acknowledge financial support from NSERC, FRQNT, and PRIMA. K.L. and V.C. acknowledge support from the NSERC Alexander Graham Bell Canada Graduate Scholarships program. R.S. acknowledges support from FRQNT for a scholarship. F.C. and G.F. acknowledge support from the Deutsche Forschungsgemeinschaft (DFG, German Research Foundation) via the Cluster of Excellence Advanced Imaging of Matter (AIM).

Disclosures. The authors declare no conflicts of interest.

Data availability. Data underlying the results presented in this paper are not publicly available at this time but may be obtained from the authors upon reasonable request.

Supplemental document. See Supplement 1 for supporting content.

REFERENCES

1. A. Kirilyuk, A. V. Kimel, and T. Rasing, "Ultrafast optical manipulation of magnetic order," *Rev. Mod. Phys.* **82**, 2731–2784 (2010).

2. Z. Tao, C. Chen, T. Szilvási, M. Keller, M. Mavrikakis, H. Kapteyn, and M. Murnane, "Direct time-domain observation of attosecond final-state life-times in photoemission from solids," *Science* **353**, 62–67 (2016).
3. P. M. Paul, E. S. Toma, P. Breger, G. Mullot, F. Augé, H. Balcou, H. G. Muller, and P. Agostini, "Observation of a train of attosecond pulses from high harmonic generation," *Science* **292**, 1689–1692 (2001).
4. A. Fleischer, O. Kfir, T. Diskin, P. Sidorenko, and O. Cohen, "Spin angular momentum and tunable polarization in high-harmonic generation," *Nat. Photonics* **8**, 543–549 (2014).
5. O. Kfir, P. Grychtol, E. Turgut, R. Knut, D. Zusin, D. Popmintchev, T. Popmintchev, H. Nembach, J. M. Shaw, A. Fleischer, H. Kapteyn, M. Murnane, and O. Cohen, "Generation of bright phase-matched circularly-polarized extreme ultraviolet high harmonics," *Nat. Photonics* **9**, 99–105 (2015).
6. C. Chen, Z. Tao, C. Hernández-García, P. Matyba, A. Carr, R. Knut, O. Kfir, D. Zusin, C. Gentry, P. Grychtol, O. Cohen, L. Plaja, A. Becker, H. Kapteyn, and M. Murnane, "Tomographic reconstruction of circularly polarized high harmonic fields," *Sci. Adv.* **2**, e1501333 (2016).
7. K. M. Dorney, L. Rego, N. J. Brooks, J. S. Román, C.-T. Liao, J. L. Ellis, D. Zusin, C. Gentry, Q. L. Nguyen, J. M. Shaw, A. Picón, L. Plaja, H. C. Kapteyn, M. M. Murnane, and C. Hernández-García, "Controlling the polarization and vortex charge of attosecond high-harmonic beams via simultaneous spin-orbit momentum conservation," *Nat. Photonics* **13**, 123–130 (2019).
8. L. Rego, K. M. Dorney, N. J. Brooks, Q. L. Nguyen, C. T. Liao, J. RománSan, D. E. Couch, A. Liu, E. Pisanty, M. Lewenstein, and L. Plaja, "Generation of extreme-ultraviolet beams with time-varying orbital angular momentum," *Science* **364**, eaaw9486 (2019).
9. P. B. Corkum, "Plasma perspective on strong-field multiphoton ionization," *Phys. Rev. Lett.* **71**, 1994–1997 (1993).
10. A. Rundquist, C. G. Durfee, III, Z. Chang, C. Herne, S. Backus, M. M. Murnane, and H. C. Kapteyn, "Phase-matched generation of coherent soft x-rays," *Science* **280**, 1412–1415 (1998).
11. T. Popmintchev, M. C. Chen, D. Popmintchev, P. Arpin, S. Brown, S. Ališauskas, G. Andriukaitis, T. Balčiūnas, O. D. Mücke, A. Pugzlys, and A. Baltuška, "Bright coherent ultrahigh harmonics in the keV x-ray regime from mid-infrared femtosecond lasers," *Science* **336**, 1287–1291 (2012).
12. D. F. Gardner, M. Tanksalvala, E. R. Shanblatt, X. Zhang, B. R. Galloway, C. L. Porter, R. Karl, Jr., C. Bevis, D. E. Adams, H. C. Kapteyn, M. M. Murnane, and G. F. Mancini, "Subwavelength coherent imaging of periodic samples using a 13.5 nm tabletop high-harmonic light source," *Nat. Photonics* **11**, 259–263 (2017).
13. J. Miao, T. Ishikawa, I. K. Robinson, and M. M. Murnane, "Beyond crystallography: diffractive imaging using coherent x-ray light sources," *Science* **348**, 530–535 (2015).
14. N. X. Truong, R. Safaei, V. Cardin, S. M. Lewis, X. L. Zhong, F. Légaré, and M. A. Denecke, "Coherent tabletop EUV ptychography of nanopatterns," *Sci. Rep.* **8**, 16693 (2018).
15. J. B. Kortright, S.-K. Kim, G. P. Denbeaux, G. Zeltzer, K. Takano, and E. E. Fullerton, "Soft-x-ray small-angle scattering as a sensitive probe of magnetic and charge heterogeneity," *Phys. Rev. B* **64**, 092401 (2001).
16. F. Siegrist, J. A. Gessner, M. Ossianer, C. Denker, Y. P. Chang, M. C. Schröder, A. Guggenmos, Y. Cui, J. Walowski, U. Martens, and J. K. Dewhurst, "Light-wave dynamic control of magnetism," *Nature* **571**, 240–244 (2019).
17. S. Valencia, A. Gaupp, W. Gudat, H.-C. Mertins, P. M. Oppeneer, D. Abramsohn, and C. M. Schneider, "Faraday rotation spectra at shallow core levels: 3p edges of Fe, Co, and Ni," *New J. Phys.* **8**, 254 (2006).
18. E. Turgut, J. M. Shaw, P. Grychtol, H. T. Nembach, D. Rudolf, R. Adam, M. Aeschlimann, C. M. Schneider, T. J. Silva, M. M. Murnane, and H. C. Kapteyn, "Controlling the competition between optically induced ultrafast spin-flip scattering and spin transport in magnetic multilayers," *Phys. Rev. Lett.* **110**, 197201 (2013).
19. E. Beaurepaire, J.-C. Merle, A. Daunois, and J.-Y. Bigot, "Ultrafast spin dynamics in ferromagnetic nickel," *Phys. Rev. Lett.* **76**, 4250–4253 (1996).
20. T. A. Ostler, J. Barker, R. F. L. Evans, R. W. Chantrell, U. Atxitia, O. Chubykalo-Fesenko, S. El Moussaoui, L. B. P. J. GuyaderLe, E. Mengotti, L. J. Heyderman, and F. Nolting, "Ultrafast heating as a sufficient stimulus for magnetization reversal in a ferrimagnet," *Nat. Commun.* **3**, 666 (2012).
21. S. Mangin, M. Gottwald, C.-H. Lambert, D. Steil, V. Uhlir, L. Pang, M. Hehn, S. Alebrand, M. Cinchetti, G. Malinowski, Y. Fainman, M. Aeschlimann, and E. E. Fullerton, "Engineered materials for all-optical helicity-dependent magnetic switching," *Nat. Mater.* **13**, 286–292 (2014).
22. S. Woo, K. M. Song, X. Zhang, M. Ezawa, Y. Zhou, X. Liu, M. Weigand, S. Finizio, J. Raabe, M.-C. Park, K.-Y. Lee, J. W. Choi, B.-C. Min, H. C. Koo, and J. Chang, "Deterministic creation and deletion of a single magnetic skyrmion observed by direct time-resolved x-ray microscopy," *Nat. Electron.* **1**, 288–296 (2018).
23. L. Caretta, M. Mann, F. Büttner, K. Ueda, B. Pfau, C. M. Günther, P. Hession, A. Churikova, C. Klose, M. Schneider, D. Engel, C. Marcus, D. Bono, K. Bagschik, S. Eisebitt, and G. S. D. Beach, "Fast current-driven domain walls and small skyrmions in a compensated ferrimagnet," *Nat. Nanotechnol.* **13**, 1154–1160 (2018).
24. I. Radu, K. Vahaplar, C. Stamm, T. Kachel, N. Pontius, H. A. Dürr, T. A. Ostler, J. Barker, R. F. L. Evans, R. W. Chantrell, A. Tsukamoto, A. Itoh, A. Kirilyuk, T. Rasing, and A. V. Kimel, "Transient ferromagnetic-like state mediating ultrafast reversal of antiferromagnetically coupled spins," *Nature* **472**, 205–208 (2011).
25. V. López-Flores, N. Bergeard, V. Halté, C. Stamm, N. Pontius, M. Hehn, E. Otero, E. Beaurepaire, and C. Boeglin, "Role of critical spin fluctuations in ultrafast demagnetization of transition-metal rare-earth alloys," *Phys. Rev. B* **87**, 214412 (2013).
26. C. E. Graves, A. H. Reid, T. Wang, et al., "Nanoscale spin reversal by non-local angular momentum transfer following ultrafast laser excitation in ferrimagnetic GdFeCo," *Nat. Mater.* **12**, 293–298 (2013).
27. J. Barker, U. Atxitia, T. A. Ostler, O. Hovorka, O. Chubykalo-Fesenko, and R. W. Chantrell, "Two-magnon bound state causes ultrafast thermally induced magnetisation switching," *Sci. Rep.* **3**, 3262 (2013).
28. R. Medapalli, I. Razdolski, M. Savoini, A. R. Khorsand, A. M. Kalashnikova, A. Tsukamoto, A. Itoh, A. Kirilyuk, A. V. Kimel, and T. Rasing, "The role of magnetization compensation point for efficient ultrafast control of magnetization in Gd₂₄Fe_{66.5}Co_{9.5} alloy," *Eur. Phys. J. B* **86**, 183 (2013).
29. A. R. Khorsand, M. Savoini, A. Kirilyuk, A. V. Kimel, A. Tsukamoto, A. Itoh, and T. Rasing, "Element-specific probing of ultrafast spin dynamics in multisublattice magnets with visible light," *Phys. Rev. Lett.* **110**, 107205 (2013).
30. W. Legrand, J.-Y. Chauleau, D. Maccariello, N. Reyren, S. Collin, K. Bouzehouane, N. Jaouen, V. Cros, and A. Fert, "Hybrid chiral domain walls and skyrmions in magnetic multilayers," *Sci. Adv.* **4**, eaat0415 (2018).
31. J.-Y. Chauleau, T. Chirac, S. Fusil, V. Garcia, W. Akhtar, J. Tranchida, P. Thibaudeau, I. Gross, C. Blouzon, A. Finco, M. Bibes, B. Dkhil, D. D. Khalyavin, P. Manuel, V. Jacques, N. Jaouen, and M. Viret, "Electric and antiferromagnetic chiral textures at multiferroic domain walls," *Nat. Mater.* **19**, 386–390 (2020).
32. M. V. Gerasimov, S. V. Ilin, M. V. Logunov, S. A. Nikitov, A. V. Spirin, and A. N. Chaldyshkin, "A magneto-optical setup for studying the time evolution of nanoscale domain-wall displacements under pulsed magnetization," *Instrum. Exp. Tech.* **60**, 716–721 (2017).
33. B. Vodungbo, A. B. Sardinha, J. Gautier, G. Lambert, M. Lozano, S. Sebban, E. Meltchakov, F. Delmotte, V. Lopez-Flores, J. Arabski, and C. Boeglin, "Table-top resonant magnetic scattering with extreme ultraviolet light from high-order harmonic generation," *Europhys. Lett.* **94**, 54003 (2011).
34. J. K. Dewhurst, F. Willems, P. Elliott, Q. Z. Li, C. von Korff Schmising, C. Strüber, D. W. Engel, S. Eisebitt, and S. Sharma, "Element specificity of transient extreme ultraviolet magnetic dichroism," *Phys. Rev. Lett.* **124**, 077203 (2020).
35. M.-C. Chen, P. Arpin, T. Popmintchev, M. Gerrity, B. Zhang, M. Seaberg, D. Popmintchev, M. M. Murnane, and H. C. Kapteyn, "Bright, coherent, ultrafast soft x-ray harmonics spanning the water window from a tabletop light source," *Phys. Rev. Lett.* **105**, 173901 (2010).
36. E. J. Takahashi, T. Kanai, K. L. Ishikawa, Y. Nabekawa, and K. Midorikawa, "Coherent water window x ray by phase-matched high-order harmonic generation in neutral media," *Phys. Rev. Lett.* **101**, 253901 (2008).
37. S. L. Cousin, T. Kanai, K. L. Ishikawa, Y. Nabekawa, and K. Midorikawa, "High-flux table-top soft x-ray source driven by sub-2-cycle, CEP stable, 185- μ m 1-kHz pulses for carbon K-edge spectroscopy," *Opt. Lett.* **39**, 5383–5386 (2014).
38. S. M. Teichmann, F. Silva, S. L. Cousin, M. Hemmer, and J. Biegert, "0.5-keV soft x-ray attosecond continua," *Nat. Commun.* **7**, 11493 (2016).

39. A. S. Johnson, D. R. Austin, D. A. Wood, C. Brahm, A. Gregory, K. B. Holzner, S. Jarosch, E. W. Larsen, S. Parker, C. S. Strüder, and P. Ye, "High-flux soft x-ray harmonic generation from ionization-shaped few-cycle laser pulses," *Sci. Adv.* **4**, eaar3761 (2018).
40. J. Li, X. Ren, Y. Yin, K. Zhao, A. Chew, Y. Cheng, E. Cunningham, Y. Wang, S. Hu, Y. Wu, M. Chini, and Z. Chang, "53-attosecond x-ray pulses reach the carbon K-edge," *Nat. Commun.* **8**, 186 (2017).
41. Y. Fu, K. Nishimura, R. Shao, A. Suda, K. Midorikawa, P. Lan, and E. J. Takahashi, "High efficiency ultrafast water-window harmonic generation for single-shot soft x-ray spectroscopy," *Commun. Phys.* **3**, 1–10 (2020).
42. J. Tate, T. Augustine, H. G. Müller, P. Salieres, P. Agostini, and L. F. DiMauro, "Scaling of wave-packet dynamics in an intense midinfrared field," *Phys. Rev. Lett.* **98**, 013901 (2007).
43. T. Nagy, S. Hädrich, P. Simon, A. Blumenstein, N. Walther, R. Klas, J. Buldt, H. Stark, S. Breittkopf, P. Jójárt, I. Seres, Z. Várallyay, T. Eidam, and J. Limpert, "Generation of three-cycle multi-millijoule laser pulses at 318 W average power," *Optica* **6**, 1423–1424 (2019).
44. B. E. Schmidt, A. Hage, T. Mans, F. Légaré, and H. J. Wörner, "Highly stable, 54mJ Yb-InnoSlab laser platform at 0.5kW average power," *Opt. Express* **25**, 17549–17555 (2017).
45. H. Fattahi, H. G. Barros, M. Gorjan, *et al.*, "Third-generation femtosecond technology," *Optica* **1**, 45–63 (2014).
46. J. Rothhardt, S. Hädrich, A. Klenke, S. Demmler, A. Hoffmann, T. Gotschall, T. Eidam, M. Krebs, J. Limpert, and A. Tünnermann, "53 W average power few-cycle fiber laser system generating soft x rays up to the water window," *Opt. Lett.* **39**, 5224–5227 (2014).
47. R. Safaei, G. Fan, O. Kwon, K. Légaré, P. Lassonde, B. E. Schmidt, H. Ibrahim, and F. Légaré, "High-energy multidimensional solitary states in hollow-core fibres," *Nat. Photonics* **14**, 733–739 (2020).
48. B. Vodungbo, J. Gautier, G. Lambert, A. B. Sardinha, M. Lozano, S. Sebban, M. Ducoussou, W. Boutu, K. Li, B. Tudu, M. Tortarolo, R. Hawaldar, R. Delaunay, V. López-Flores, J. Arabski, C. Boeglin, H. Merdji, P. Zeitoun, and J. Lüning, "Laser-induced ultrafast demagnetization in the presence of a nanoscale magnetic domain network," *Nat. Commun.* **3**, 999 (2012).
49. B. Pfau, S. Schaffert, L. Müller, *et al.*, "Ultrafast optical demagnetization manipulates nanoscale spin structure in domain walls," *Nat. Commun.* **3**, 1100 (2012).
50. E. Prieto, F. Heigl, O. Krupin, G. Kaindl, and K. Starke, "Magneto-optics of Gd and Tb in the soft x-ray resonance regions," *Phys. Rev. B* **68**, 134453 (2003).
51. E. Constant, D. Garzella, P. Breger, E. Mével, C. Dorrer, C. Le Blanc, F. Salin, and P. Agostini, "Optimizing high order harmonic generation in absorbing gases: model and experiment," *Phys. Rev. Lett.* **82**, 1668–1671 (1999).
52. J. Rothhardt, M. Krebs, S. Hädrich, S. Demmler, J. Limpert, and A. Tünnermann, "Absorption-limited and phase-matched high harmonic generation in the tight focusing regime," *New J. Phys.* **16**, 033022 (2014).
53. M. Schnürer, C. Spielmann, P. Wobrauschek, C. Strelt, N. H. Burnett, C. Kan, K. Ferencz, R. Koppitsch, Z. Cheng, T. Brabec, and F. Krausz, "Coherent 0.5-keV x-ray emission from helium driven by a sub-10-fs laser," *Phys. Rev. Lett.* **80**, 3236–3239 (1998).
54. E. A. Gibson, A. Paul, N. Wagner, R. Tobey, D. Gaudiosi, S. Backus, I. P. Christov, A. Aquila, E. M. Gullikson, D. T. Attwood, and M. M. Murnane, "Coherent soft x-ray generation in the water window with quasi-phase matching," *Science* **302**, 95–98 (2003).
55. C. Spielmann, N. H. Burnett, S. Sartania, R. Koppitsch, M. Schnürer, C. Kan, M. Lenzner, P. Wobrauschek, and F. Krausz, "Generation of coherent x-rays in the water window using 5-femtosecond laser pulses," *Science* **278**, 661–664 (1997).
56. K. Hong, C.-J. Lai, J. P. Siqueira, P. Kroger, J. Moses, C.-L. Chang, G. J. Stein, L. E. Zapata, and F. X. Kärtner, "Chirped-pulse amplifier and high-flux soft x-ray high-harmonic generation," *Opt. Lett.* **39**, 3145–3148 (2014).
57. A. Paul, E. A. Gibson, X. Zhang, A. Lytle, T. Popmintchev, X. Zhou, M. M. Murnane, I. P. Christov, and H. C. Kapteyn, "Phase-matching techniques for coherent soft x-ray generation," *IEEE J. Quantum Electron.* **42**, 14–26 (2006).
58. V. Cardin, T. Balciunas, K. Légaré, A. Baltuska, H. Ibrahim, E. Jal, B. Vodungbo, N. Jaouen, C. Varin, J. Lüning, and F. Légaré, "Wavelength scaling of ultrafast demagnetization in Co/Pt multilayers," *Phys. Rev. B* **101**, 054430 (2020).
59. A. E. D. Merhe, "Ultrafast modification of the magnetic anisotropy in a CoTb alloy," Ph.D. Thesis (Sorbonne Université, 2019).
60. T. Ferté, N. Bergeard, G. Malinowski, R. Abrudan, T. Kachel, K. Holldack, M. Hehn, and C. Boeglin, "Ultrafast hot-electron induced quenching of Tb 4f magnetic order," *Phys. Rev. B* **96**, 144427 (2017).
61. T. Fan, P. Grychtol, R. Knut, *et al.*, "Bright circularly polarized soft x-ray high harmonics for x-ray magnetic circular dichroism," *Proc. Natl. Acad. Sci. USA* **112**, 14206–14211 (2015).
62. M. Elzo, E. Jal, O. Bunau, S. Grenier, Y. Joly, A. Y. Ramos, H. C. N. Tolentino, J.-M. Tonnerre, and N. Jaouen, "X-ray resonant magnetic reflectivity of stratified magnetic structures: eigenwave formalism and application to a W/Fe/W trilayer," *J. Magn. Magn. Mater.* **324**, 105–112 (2012).
63. J. P. Hannon, G. T. Trammell, M. Blume, and D. Gibbs, "X-ray resonance exchange scattering," *Phys. Rev. Lett.* **61**, 1245–1248 (1989).
64. P. Salieres, B. Carré, L. Le Déroff, F. Grasbon, G. G. Paulus, H. Walther, R. Kopold, W. Becker, D. B. Milosevic, A. Sanpera, and M. Lewenstein, "Feynman's path-integral approach for intense-laser-atom interactions," *Science* **292**, 902–905 (2001).
65. R. A. Bartels, A. Paul, H. Green, H. C. Kapteyn, M. M. Murnane, S. Backus, I. P. Christov, Y. Liu, D. Attwood, and C. Jacobsen, "Generation of spatially coherent light at extreme ultraviolet wavelengths," *Science* **297**, 376–378 (2011).
66. O. Kfir, N. Xuan, R. Safaei, V. Cardin, S. M. Lewis, X. L. Zhong, F. Légaré, and M. A. Denecke, "Nanoscale magnetic imaging using circularly polarized high-harmonic radiation," *Sci. Adv.* **3**, eaao4641 (2017).
67. B. Koopmans, G. Malinowski, F. D. Longa, D. Steiauf, M. Fähnle, T. Roth, M. Cinchetti, and M. Aeschlimann, "Explaining the paradoxical diversity of ultrafast laser-induced demagnetization," *Nat. Mater.* **9**, 259–265 (2009).
68. J. W. Kim, K. D. Lee, J. W. Jeong, and S. C. Shin, "Ultrafast spin demagnetization by nonthermal electrons of TbFe alloy film," *Appl. Phys. Lett.* **94**, 192506 (2009).
69. A. Eschenlohr, M. Sultan, A. Melnikov, N. Bergeard, J. Wiecek, T. Kachel, C. Stamm, and U. Bovensiepen, "Role of spin-lattice coupling in the ultrafast demagnetization of Gd_{1-x}Tb_x alloys," *Phys. Rev. B* **89**, 214423 (2014).
70. M. Van Veenendaal and I. McNulty, "Prediction of strong dichroism induced by x rays carrying orbital momentum," *Phys. Rev. Lett.* **98**, 157401 (2007).
71. W. Yang, H. Yang, Y. Cao, and P. Yan, "Photonic orbital angular momentum transfer and magnetic skyrmion rotation," *Opt. Express* **26**, 8778–8790 (2018).
72. S. Zhang, Z. Fu, B. Zhu, G. Fan, Y. Chen, S. Wang, Y. Liu, A. Baltuska, C. Jin, C. Tian, and Z. Tao, "Solitary beam propagation in periodic layered Kerr media enables high-efficiency pulse compression and mode self-cleaning," *Light Sci. Appl.* **10**, 53 (2021).